HHS Public Access

Author manuscript

Science. Author manuscript; available in PMC 2021 September 22.

Published in final edited form as:

Science. 2021 April 23; 372(6540): . doi:10.1126/science.abe1931.

Cholinergic neurons engage the integrated stress response for dopamine modulation and skill learning

Ashley R. Helseth[†,1], **Ricardo Hernandez-Martinez**[†,1], **Victoria L. Hall**[2], **Matthew L. Oliver**[3], **Brandon D. Turner**[1], **Zachary F. Caffall**[1], **Joseph E. Rittiner**[1], **Miranda K. Shipman**[1], **Connor S. King**[1], **Viviana Gradinaru**[4], **Charles Gerfen**[5], **Mauro Costa-Mattioli**[6], **Nicole Calakos**[1,2,3,7,*]

[1]Department of Neurology, Duke University Medical Center, Durham, North Carolina 27715, USA

[2]Departments of Neurobiology, Duke University Medical Center, Durham, North Carolina 27715, USA

[3]Department of Cell Biology, Duke University Medical Center, Durham, North Carolina 27715, USA

[4]Division of Biology and Biological Engineering, California Institute of Technology, Pasadena, California 91125, USA

[5]National Institute of Mental Health, Section on Neuroanatomy, Bethesda, Maryland 20892, USA

[6]Department of Neuroscience, Baylor College of Medicine, Houston, Texas 77030, USA

[7]Duke Institute for Brain Sciences, Durham, North Carolina 27715, USA

Abstract

The integrated stress response (ISR) maintains proteostasis by modulating protein synthesis and is important in synaptic plasticity, learning and memory. We developed a reporter (SPOTlight) for brain-wide imaging of ISR state with cellular resolution. Unexpectedly, we found a class of neurons in mouse brains, striatal cholinergic interneurons (CINs), in which the ISR was activated at steady-state. Genetic and pharmacological manipulations revealed that ISR signaling was necessary in CINs for normal type 2 dopamine receptor (D2R) modulation. Inhibiting the ISR inverted the sign of D2R modulation of CIN firing and evoked dopamine release and altered skill

[*]Corresponding Author: nicole.calakos@duke.edu.

Author contributions: A.R.H. performed majority of SPOTlight imaging, DREADD manipulation, immunohistochemical experiments, and data analysis, and designed behavioral experiments and analyzed results from core facility for MWM, OFT, rotarod, and fear conditioning; V.L.H. designed, supervised, and analyzed lever press CReP studies; R.H.M. initiated study of ISR in CINs and designed, performed, and analyzed all CIN recording experiments; M.O. contributed to SPOTlight validation and imaging analyses, designed and analyzed p-PERK immunohistochemical measures; Z.C., J.E.R. conceived of and designed SPOTlight reporter; B.D.T. designed, performed, and analyzed dLight experiments; M.K.S. performed all viral surgeries and a subset of immunohistochemical staining, and documented viral spread for DREADD and CReP experiments; C.S.K. performed single-cell RNA sequencing analysis; V.G. advised on project and contributed unpublished reagents; C.G. participated in early SPOTlight image analyses and interpretations; M.C.-M. contributed conceptually and supervised R.H.M. during *Eif2s1* phosphomutant studies; A.R.H. and N.C. wrote manuscript with significant input from all authors; N.C. participated in conceptual development, research oversight, and interpretation.

[†]equal contribution

Competing interests: The authors have no competing interests to disclose.

Data and materials availability: All data are available in the manuscript or the supplemental material. Plasmids will be made available through Addgene or upon request.

learning. Thus, a non-canonical, steady-state mode of ISR activation is found in CINs and the ISR plays a neuromodulatory role in learning.

Graphical Abstract

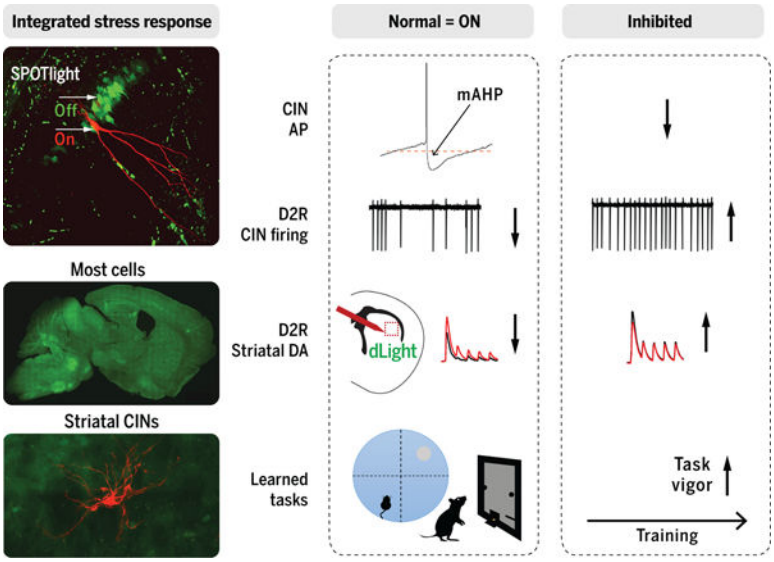

One sentence summary:

Striatal cholinergic interneurons have high steady-state ISR activation that regulates dopamine modulation and skill learning.

The integrated stress response (ISR) is a highly conserved mechanism for cells to restore homeostasis in the face of diverse stressors, from unfolded proteins to nutrient deficiencies (1, 2). In the brain, regulation of protein synthesis by the ISR pathway is also required for long-term memory and synaptic plasticity (3–5). These key roles in the cellular stress response and learning and memory have attracted significant attention to the potential for the ISR as a therapeutic target in a wide range of human diseases including cognitive, neurodegenerative, movement, and substance use disorders (6–15).

Under healthy conditions, ISR signaling has canonically been understood as a temporary process controlled by the phosphorylation state of eukaryotic initiation factor 2 alpha (eIF2α). Eukaryotic IF2 is a ternary complex of α, β, and γ subunits that is required for protein synthesis initiation by enabling the binding of methionyl-tRNA to the ribosome in a GTP-dependent manner. Four dedicated eIF2α kinases (PERK, HRI, PKR, and GCN2) respond to different stressors by phosphorylating eIF2α at serine 51 (16). Kinase activity is balanced by two phosphatase complexes that share a common catalytic core, protein phosphatase 1 (PP1), but contain different regulatory subunits (GADD34 or CReP) that confer specificity for eIF2α. Phosphorylation of eIF2α causes dramatic shifts in protein synthesis. The bulk of protein synthesis is decreased; however, this overall reduction is accompanied by increased translation of a subset of mRNAs that contain upstream open reading frames (uORFs), most notably ATF4 (1, 17–19).

While the translational consequences of ISR activation may have enduring effects dictated by the half-lives of the newly synthesized proteins, under normal conditions eIF2α phosphorylation itself is transient. To date, conventional approaches such as immunohistochemistry (IHC) have failed to capture these dynamic ISR signaling events, and present technical challenges including low throughput and modest antibody performance. To overcome this problem, we developed a reporter to reveal the translational state of the ISR pathway in brain cells.

With this reporter, we made the surprising discovery that, in contrast to the usual paradigm of stressor/stimulus-induced ISR activation, the ISR was constitutively activated in a subset of CNS neurons, striatal cholinergic interneurons (CINs). Using cell-selective manipulations, we then showed that the level of CIN ISR activation was activity-dependent, determined how D2R modulates CIN firing and striatal dopamine release, and changed performance of learned tasks. Our CIN-specific behavioral effects also reproduced some of the findings previously described with systemic ISR inhibition (20–22), indicating that ISR signaling in neuromodulatory cells is at least one of the cellular targets contributing to the enhanced learning effects associated with ISR inhibition.

SPOTlight reporter measures ISR state-dependent protein synthesis

We aimed to create a reporter with single-cell resolution that conveys information about the relative abundance of translation driven by eIF2α in its phosphorylated and unphosphorylated forms – essentially creating a thermometer-like scale for eIF2α phospho-state-dependent contributions to the proteome. Because activation of the ISR leads to differential usage of uORFs in the 5’ UTR of *Atf4* mRNA (19, 23), we inserted green and red fluorophores into distinct but overlapping reading frames. With this design, one of the two fluorophores would be translated, mutually exclusively, based on ISR activation state (Fig. 1A). We named the reporter SPOTlight, for Selective Phospho-eIF2α ORF Tracking light. SPOTlight expresses tdTomato from the *Atf4* start codon, which is translated when the ISR is activated (high p-eIF2α). The coding sequence for a contrasting fluorophore, EGFP, was placed in uORF2, which is translated under conditions of low p-eIF2α. Thus, using a single reporter we could monitor translation when the ISR was activated or inactive. We then packaged the reporter construct into an AAV bearing the PHP.eB capsid to allow efficient brain-wide transduction in mice after a simple retro-orbital injection (24) (Fig. 1B). Importantly, *Atf4* mRNA is ubiquitously expressed throughout the body, and *Atf4* regulatory uORFs are conserved from invertebrates to mammals (17, 18). Thus, the SPOTlight reporter can be adapted for use in a wide array of species and contexts after simple changes to viral packaging and delivery.

We expected that the non-phosphorylated eIF2α state would predominate under basal conditions, and lead to EGFP translation and green fluorescence. In contrast, increased translation of tdTomato would be expected when eIF2α is phosphorylated, such as under conditions activating the ISR (17, 18). Indeed, brain-wide, the SPOTlight EGFP signal predominated, whereas tdTomato signal was lower, even when amplified by anti-RFP labeling (Fig. 1C, D). Although rare, occasional cells with significant red fluorescence were found, for example, among hippocampal pyramidal neurons and cerebellar Purkinje cells

(Fig. 1E). These sparse cells likely reflected stochastic ISR pathway activation owing to cell stress or other activators.

To test the relationship between SPOTlight fluorophore expression, ISR activation, and eIF2α phosphorylation, SPOTlight-expressing mice were treated with tunicamycin (Tm), a potent activator of the PERK branch of the ISR (Fig. 1B). As expected, acute systemic in vivo Tm exposure significantly increased tdTomato fluorescence 8 hr post-injection (Fig. 1F,G; Tm: 296.7 ± 45.7% of Veh, p=0.0015), consistent with predictions that eIF2α phosphorylation levels would rise after an ISR trigger (1). To establish whether the Tm-evoked tdTomato increase required p-eIF2α, we used a pharmacological inhibitor, ISRIB, which blocks the downstream translational effects of eIF2α phosphorylation (20, 25). When ISRIB was given prior to Tm, tdTomato intensity was significantly lower (Fig. 1F,G; Tm: 296.7 ± 45.7% of Veh v. ISRIB/Tm 126.6 ± 34.3% of Veh, p = 0.0242), while administration of ISRIB alone did not significantly alter tdTomato levels compared to vehicle control (Fig. S1A-C; 78.9 ± 14.4% of Veh, p=0.4269). The potent ISR induction by Tm also provided an ideal opportunity to establish the relationship between tdTomato intensity and p-eIF2α (ISR activation) levels. p-eIF2α levels increased in parallel with tdTomato signal in virally transduced cells (Fig. 1F, Fig. S2; Tm: 149.9 ± 10.3% of Veh, p=0.0001; Pearson correlation coefficient r=0.8296). We found no significant difference in p-eIF2α immunofluorescence between vehicle and ISRIB alone (Fig. S1C; p=0.5142). Thus, as predicted, SPOTlight mRNA translation was controlled by the ISR.

Tonically active cholinergic interneurons show steady-state ISR activation

In the striatum, we observed that the sparse red cells did not seem to be stochastic (as observed in CA2 and Purkinje cells), but rather corresponded to a specific cell subtype that uniformly and strongly expressed SPOTlight tdTomato. Based on their distinctive morphology, we suspected these cells might be striatal cholinergic interneurons (CINs) and performed IHC with a cholinergic interneuron-specific marker, choline acetyltransferase (ChAT). Indeed, although striatal projection neurons (SPNs) were successfully transduced by AAV-PHP.eB (Fig. S3), tdTomato signal was highly correlated with expression of choline acetyltransferase (ChAT), but not the SPN marker DARPP32 (Fig. 2A). To further support these findings, we directly measured p-eIF2α levels in CINs and SPNs by IHC. Cytoplasmic p-eIF2α intensity was elevated more than 25-fold in CINs (ChAT+) compared to SPNs (DARPP32+) (Fig. 2B-C). To assess how widespread elevated p-eIF2α levels were among CINs, we defined “background” p-eIF2α intensity as the mean value observed in SPNs. Compared to this baseline, greater than 90% of CINs, but less than 5% of SPNs, had elevated p-eIF2α (>2 SD; n= 92 CINs and 395 SPNs from three C57Bl/6 mice). Significant differences between CINs and SPNs were also observed using measures of two other ISR components – upstream activation of the PERK branch of the ISR, and the downstream consequences on *Atf4* transcription (Fig. S4). Thus, the high SPOTlight-tdTomato signal in CINs corresponded with multiple measures of ISR pathway activity, supporting the unexpected conclusion that in CINs, the ISR was constitutively activated at steady state.

Relative to other striatal neurons, CINs are notable for their tonic action potential firing. Because increased neuronal activity is the presumptive trigger for eIF2α phosphorylation

during synaptic plasticity (4), we hypothesized that tonic action potential firing in CINs might be the cellular trigger for ISR activation. To test this hypothesis, we chronically suppressed CIN activity using the inhibitory DREADD hM4Di (26, 27). Briefly, ChAT-Cre mice were transduced with AAVs that Cre-dependently express hM4Di-mCherry or mCherry alone. After administering the DREADD-specific ligand, clozapine N-oxide (CNO), twice daily for 5 days, IHC revealed that $G_{i/o}$ DREADD activity significantly reduced p-eIF2α and p-PERK levels in CINs compared to the mCherry control (Fig. 2D-E and Fig. S4, respectively). Thus, CIN activity is a driver of steady-state ISR activation in these cells.

To survey whether there were other neuronal subtypes with high basal ISR demand, we used SPOTlight and found a tendency for other high-firing cell types to have higher proportions of cells with red-dominant SPOTlight signal, but none had a cell class-wide effect like CINs (Fig. S5). Although the AAV PHP.eB serotype is useful to easily sample neurons and glia brain-wide, our cell survey is limited to its viral tropism. For other specific cell populations, dedicated studies delivering SPOTlight with methods that efficiently target those cells will be necessary.

ISR state of cholinergic interneurons determines sign of CIN D2R modulation

We next sought to understand the functional significance of constitutive ISR activation in CINs. The ISR is known to be required for long-lasting forms of synaptic plasticity (3, 4, 28), including long-term depression at cortico-striatal synapses on striatal projection neurons (c-s LTD) (6). Modulation of CIN activity via the type 2 dopamine receptor (D2R) is also required for the induction of c-s LTD at SPN synapses (29, 30). D2R signaling transiently lowers tonic CIN action potential firing (31) and this D2R-mediated “pause” is thought to play a necessary and permissive role for induction of c-s LTD in SPNs (32, 33). These associations led us to wonder whether pharmacological and genetic inhibition of the ISR would affect D2R-mediated modulation of CINs.

To answer this question, we performed cell-attached recordings of CINs in acute brain slices and evaluated responses to the D2R agonist, quinpirole (QUIN) (Fig. 3A,B). Compared to control slices (VEH), slices pre-incubated with the ISR inhibitor, ISRIB, showed significant differences in QUIN rate modulation (Fig. 3C-E). This QUIN effect was blocked by the D2R antagonist, sulpiride (Fig. S6), which suggests that it involved D2R actions.At the group level, ISRIB caused a net increase in CIN firing, effectively inverting the sign of D2R modulation (Fig. 3E). Consistent with these results, the PERK antagonist, AMG PERK 44, also inverted the normal D2R response (Fig. 3F-H). We next tested the D2R response in phospho-mutant *Eif2s1*$^{S/A}$ mice, which exhibit a genetic haplo-insufficiency for the eIF2α phosphorylation site (S51A) (34) and reduced brain levels of p-eIF2α (*21*). Accordingly, genetic inhibition of the ISR also caused a net increase in CIN firing rate in response to QUIN (Fig. S7). Thus, genetic or pharmacological inhibition of the ISR profoundly changes the nature of D2R modulation of CIN firing by causing a rate increase instead of decrease.

Because a full understanding of how the ISR regulates neuromodulatory state requires its dissection at the cellular level, we developed a molecular genetic approach to inhibit the ISR in a cell-type specific manner. The p-eIF2α phosphatase, CReP, was expressed in a Cre-dependent manner using a viral vector (AAV-DIO-CReP; see Fig. 3A schematic for CReP in ISR pathway). We then injected AAV-DIO-CReP into the dorsal striatum of ChAT-Cre mice (Fig. 3I). Using p-eIF2α IHC, we first confirmed that expression of CReP in this manner was sufficient to lower p-eIF2α levels in CINs (Fig. 3J,K). We then tested responses to quinpirole and found that CReP overexpression in CINs disrupted D2R modulation similarly to the global pharmacological and genetic manipulations (Fig. 3L-N). Lastly, although some ISR manipulations altered basal CIN firing rates (e.g. Fig. 3D lowers, Fig. 3M increases), there was no consistent relationship between basal firing rates that could explain D2R CIN modulation effects (Fig. S8). Thus, ISR activity is specifically required within CINs for normal D2R modulation of CIN firing.

We next examined which CIN conductances might be altered by ISR activity to cause the D2R-dependent CIN firing differences. Using whole cell current-clamp recordings to examine current-voltage (I-V) relationships, we surveyed properties of intrinsic membrane excitability and action potential (AP) waveforms (Table S1). ISR inhibition by ISRIB reduced the magnitude and duration of the medium afterhyperpolarization (mAHP) component of the AP (Fig. S9A-C, Table S1). We thus hypothesized that the ISR may regulate SK channel activity because SK channels are the major contributor to the mAHP in CINs (35, 36). To directly test the role of SK channels, we bidirectionally manipulated SK channel activity. First, we tested the effects of an SK channel antagonist, apamin, on the D2R response of CINs. Apamin was sufficient to reproduce the D2R response inversion associated with ISR inhibiting manipulations (Fig. S9D-F). To test whether reduced SK activity was required for ISRIB's actions, we compared ISRIB's actions in the presence or absence of an SK channel positive allosteric modulator, CyPPA. CyPPA significantly blocked ISRIB's effects, indicating that SK activity reduction is also necessary (Fig. S9G-I). Thus we suggest a molecular model in which the ISR regulates SK channel activity and the mAHP to influence the CIN firing response to D2R agonism.

We next examined whether CIN ISR activity had consequences on striatal dopamine release because striatal cholinergic signaling is a well-known regulator of dopamine release (37). Evoked dopamine (DA) transients were detected using the dLight1.2 fluorescent reporter (38) in response to intra-striatal electrical stimulation in acute brain slices. In control slices, D2R antagonism by sulpiride increased evoked dLight responses (Fig. 4B), indicating that the net effect of striatal D2R contributions was to depress DA release (Fig. 4C,D). In marked contrast, sulpiride reduced evoked dopamine transients in ChAT Cre/DIO-CReP slices (Fig. 4B), indicating that when the ISR was inhibited in CINs, the net D2R effect was to enhance DA release (Fig. 4C,D). These results are consistent with what would be predicted from the known effects of CIN activity on dopamine release (37, 39) combined with our finding that ISR inhibition causes D2R signaling to increase, rather than decrease, CIN firing (Fig. 3). Thus, genetic, pharmacological, and cell-specific manipulations clearly demonstrate that ISR activity in CINs is necessary for the integrity of dopamine D2R modulation, with both cell autonomous and circuit-level consequences.For both effects ISR inhibition effectively inverts the normal sign of D2R-mediated modulation.

ISR state of CINs regulates skill learning

Striatal integration of cholinergic and dopaminergic signaling is central to sensorimotor learning and motor skill performance (32, 40). In prior studies, enhanced performance in learning tasks has been observed with systemic or brain-wide ISR inhibition (20–22). We thus asked whether ISR activity in CINs might be a target for some of these behavioral outcomes. Accordingly, we genetically lowered ISR activity in dorsal striatal cholinergic interneurons by injecting AAV-DIO-CReP or control AAV into the dorsal striatum of ChAT-Cre mice (Fig 5A). Viral spread was documented post-mortem and expression within ChAT+ cells confirmed by IHC for the Myc-tag and p-eFI2α (Fig. S10).

Following three weeks of viral expression, mice were tested using the same Morris water maze (MWM) training protocol that previously showed enhanced learning with systemic ISRIB treatment (20). Mice with CIN-CReP overexpression reached the hidden platform faster (Fig. 5B), reproducing results from prior systemic genetic and pharmacological ISR manipulations (20–22). We further found that the effect was sex-dependent (males only) (Fig. S11) and prior reports were of all male cohorts (20–22). Lastly, memory effects measured by the probe test performed on day 3 of training showed similar trends as prior reports but suffer from being underpowered owing to the sexually divergent effects (Fig. S11). We thus tested independent cohorts of mice using an orthogonal assay for motor skill learning, a lever press task that we have not found to have significant sex-related effects (41). Mice were trained to press a lever for a food pellet reward through a series of increasingly delayed reward contingencies, as previously described (41). In the lever press task, CIN-CReP overexpressing mice again outperformed control mice, showing higher lever press rates (Fig. 5C and S12). Furthermore, the performance differences once again emerged over time and were not present at the onset of training, consistent with effects on skill learning.

The specific lever press training protocol we used promotes habit learning (41) and lever press rates can be influenced by training paradigms associated with goal-directed or habitual behavior (42, 43). We thus tested whether deficits in habit learning might explain the learning curve differences. To this end, we employed a probe test for habitual behavior, which measures the persistence of lever pressing when the reward is absent and has been devalued by pre-feeding. However, we found no evidence for any effects of CIN-specific CReP overexpression on habit learning (Fig. 5D). We also found that CIN-CReP overexpression in the targeted dorsal striatal region did not alter rotarod performance or fear conditioning (Fig. S13).

Given known contributions of dopamine and dorsal striatal circuits to performance vigor (44, 45), we wondered whether the performance effects in the Morris water maze and lever press task might relate to a common effect on speed/vigor. We performed sub-analyses to address this possibility and found that the Morris water maze results did appear to be driven by effects on swim velocity. Male CIN-CReP OE mice learned to swim with higher velocities than controls (Fig. 5F). We also found that the faster lever press rates that emerged with training in CIN-CReP OE mice were accompanied by a skewed distribution towards shorter inter-press intervals (Fig. 5E). Lastly, we examined whether the mice were

hyperactive in general, by monitoring locomotion in an open field (OF) apparatus. In contrast to the behavioral differences that emerged in the skill learning tasks, CIN-CReP overexpression had no effect on locomotor speed in an untrained, exploratory behavior test (Fig. 5G). Thus, ISR signaling in striatal cholinergic interneurons influences the vigor of learned tasks. In addition, because our CIN-specific results reproduce some behaviors previously elicited by systemic ISR inhibition, striatal cholinergic interneurons represent an underlying cellular target for at least some of the learning enhancement effects.

Conclusions

Here we discovered a role for the ISR in brain function -- neuromodulation. ISR activity in CINs powerfully regulates dopamine modulation and learned skill. Furthermore, we found that striatal cholinergic interneurons as a class are distinct from most neurons in that they show constitutive activation of the integrated stress response. This basal ISR activation in CINs is dependent on tonic firing activity. CIN ISR signaling influences the D2R-mediated firing response by establishing basal intrinsic membrane excitability properties. The consequences of CIN ISR signaling markedly shape D2R-mediated dopamine release in striatal circuits, and the degree of vigor in learned task performance.

By developingSPOTlight to assess ISR state-dependent translation brain-wide (, we were initially led to the surprising discovery of rare cell types with high levels of ISR activation at steady state. The existence of cell types with a chronic basal demand for ISR activity carries significant implications for their potential vulnerability to ISR-inhibiting states, whether due to environmental, genetic, or pharmacological causes. Moreover, sex differences observed with CIN ISR inhibiting manipulations in both behaviors suggest that sexually dimorphic biology may determine sensitivity to ISR state.

Although we focus on cholinergic interneurons in this study because CINs show a striking population-wide engagement of the ISR basally, SPOTlight revealed a number of other cell types with at least portions of the population denoting ISR activation. Examining the significance of ISR activation in these cell subsets may reveal additional ISR roles. Indeed, recent studies in circadian rhythms and axon guidance highlight the potential for more diverse neuronal roles of ISR signaling in the brain (10, 46). Our conclusions regarding the behavioral significance of the ISR in CINs are restricted to the portion of dorsal striatal cholinergic neurons manipulated. Manipulating the ISR in other cholinergic populations will be necessary to test additional contributions, such as to motivational salience in ventral striatal populations (47, 48). Lastly, the ISR has been variously implicated as a candidate mechanism and/or therapeutic target for a number of human diseases, including dystonia, neoplastic, neurodegenerative, and cognitive disorders (6–15, 49). In such disease states, SPOTlight may help identify critical sites and time windows of ISR dysregulation.

Our findings expand the understanding of where and how the ISR acts to influence learning and memory behavior. The ISR plays a steady-state role in striatal CINs that determines the neuromodulatory state of the striatal circuitry, with behavioral consequences that negatively constrain the vigor of learned tasks. ISR inhibition has previously been associated with enhanced task learning and long-term potentiation (LTP). Here we show that ISR activity

in striatal cholinergic neurons underlies at least some of the enhanced learning effects of systemic ISR inhibition (20–22). In addition, interpretation of the ISR site of action for long-term synaptic plasticity has focused on mechanisms such as local regulation of protein synthesis in the potentiated/depressed cell (4, 28, 50). However, given that many forms of synaptic plasticity and learning and memory are heavily influenced by neuromodulation from dopamine and/or acetylcholine (29, 51–54), our results prompt further examination of the exact cellular sites of action for the ISR in various forms of synaptic plasticity and learned behaviors.

Materials and Methods

Animals

All experimental procedures were approved by the Institutional Animal Care and Use Committee at Duke University. Sample size was based on the ARRIVE recommendations. All animals were maintained on a 12:12 light-dark cycle with ad libitum access to food and water. C57Bl/6J mice and IRES-Cre ChAT-Cre mice (JAX: 006410) were obtained from Jackson laboratories. *Eif2s1* S51A mice (34) were maintained on a C57Bl/6J background. For slice-electrophysiology, homozygous IRES ChAT-Cre mice were crossed with homozygous Ai3 reporter mice on the Rosa26 locus (JAX: 007903) to yield double heterozygotes with EYFP-expressing cholinergic interneurons. Juvenile (P21–60) male and female mice were utilized for slice electrophysiology; whereas, adult male and female mice aged 10–12 weeks were used for viral injections, and subsequent behavior or immunohistochemistry was performed on mice aged 14–25 weeks.

Genotyping

Toes were collected between P7-P14 for genotyping and the following primers were used:

Ai3: WT forward 5’-AAG GGA GCT GCA GTG GAG TA-3’; WT reverse 5’-CCG AAA ATC TGT GGG AAG TC-3’; Mutant forward 5’ACA TGG TCC TGC TGG AGT TC-3’; Mutant reverse 5’-GGC ATT AAA GCA GCG TAT CC-3’. *Eif2s1* (S51A): Forward: 5’CAC ACA CCC ATT CCA TGA TAG TAA ATG-3’; Reverse 5’-CAA TGT TGT AGA CCC TGA CAA TGA AGG-3”. Sequencing for ChAT-Cre genotype was performed by Transnetyx, Inc (Cordova, TN) using real-time PCR according to methods described in (55).

Viral Constructs

The recombinant Adeno-associated viral (AAV) construct, SPOTlight was developed in the lab consisting of recombinant DNA manufactured based on the known published sequence of murine activating transcription factor 4 (*Atf4*) mRNA (NCBI Reference Sequence: NM_009716.3) by Vector Builder (https//en.vectorbuilder.com/) and cloned into an AAV vector carrying the CMV early enhancer/chicken beta-actin (CAG) promoter. The vector construct was then packaged into a PHP.eB capsid (24) by the Duke Viral Vector Core. The final concentration was 3.0×10^{13} genome copies per mL. An AAV vector construct containing the EGFP fluorophore with the CAG promotor packaged in the PHP.eB capsid, viral concentration 2.0×10^{13} genome copies per mL, was used as a control.

The Cre-activated recombinant AAV-construct, AAV5-hSYN-DIO-mCReP termed “CReP OE” virus, was developed in the lab and packaged by the Duke Viral Core. A double-floxed inverted orientation (DIO) construct was synthesized containing two pairs of incompatible Lox sites (LoxP and Lox2722) and the Ppp1r15b gene manufactured based on the known published sequence of mouse protein phosphatase 1, regulatory subunit 15b (*Ppp1r15b*) mRNA (NCBI Reference Sequence: NM_133819.3) by Vector Builder (https://en.vectorbuilder.com/) was inserted between the LoxP and Lox2722 sites in the reverse orientation, and cloned into a vector carrying the neuronal-specific human synapsin 1 (hSYN) gene promotor. The new vector construct underwent quality control testing with DNA quantification, restriction enzyme digestion, and Sanger sequencing. The resulting vector was then serotyped with AAV5 coat proteins and packaged by the Duke Viral Vector Core. The final viral concentration was 1.0×10^{13} genome copies per mL.

Viral Injections

AAV-PHP.eB-CAG-SPOTlight virus was administered by retro-orbital injection in 10–12 week old C57Bl/6J mice that were anesthetized with isoflurane until absent paw-pinch response and then rapidly injected behind the orbit with 10 μL of virus diluted in 40 μL of 0.2 micron sterile-filtered phosphate-buffered saline (PBS) for a total injection volume of 50 μL with a single use 0.5 mL insulin syringe (BD) and then monitored through recovery from anesthesia for return to normal activity. Post-procedure analgesia with one to two drops of Bupivacaine ophthalmic solution was applied.

Ten to twelve-week-old ChAT-Cre heterozygous mice received either an intracranial injection of double floxed reversed rAAV5-hSYN-DIO-mCReP at a 3:1 dilution with rAAV5-Ef1a-mCherry virus or control (3:1 dilution of 1× PBS vehicle to rAAV5-Ef1a-mCherry virus). For stereotactic viral injections, mice were anesthetized with isoflurane and maintained under anesthesia during the entire procedure. While under anesthesia, mice were monitored visually, and depth of sedation ensured by absence of response to paw pinch. 600 nL of virus was injected per hemisphere into the dorsal striatum (anteroposterior +0.5 mm and 2 mm mediolateral from bregma) at two depths of −2.5 mm and −3.0 mm with a Nanoject III Programmable Nanoliter Injector at 2.5 nL per second. Experiments including behavioral analysis and immunohistochemistry were carried out three weeks later to allow for viral expression.

In vivo drug treatments

Tunicamycin dissolved in DMSO (5 mg/mL) was purchased from Millipore Sigma (St. Louis, MO) and diluted 1:25 (vol/vol) in 150 mM Dextrose to administer a final concentration of 3 μg/g bodyweight per mouse in a single i.p. dose. Vehicle controls were injected i.p. with 0.2 micron sterile-filtered DMSO diluted 1:25 (vol/vol) in 150 mM Dextrose. Trans-ISRIB was purchased from Tocris Biosciences (Minneapolis, MN) dissolved in DMSO to 5 mM and then further diluted 1:10 (vol/vol) in 0.2 micron sterile-filtered 1× PBS with Tween-80 to administer a final concentration of 2.5 mg/kg per mouse delivered by i.p. injection one hour prior to injection with tunicamycin or vehicle (1:10 vol/vol DMSO to 1× PBS with Tween-80).

Immunohistochemistry (IHC)

For preparation of brain tissue for IHC, mice were anesthetized by aerosolized isoflurane and i.p. injection of 250 mg/kg Tribromoethanol (Avertin), followed by opening of the thoracic cavity and transcardial perfusion with 1× PBS followed by fixation with 4% paraformaldehyde. Perfused brains were carefully removed and stored in 4% PFA overnight, followed by 48 hours in 30% sucrose solution in 1× PBS for cryoprotection. Brains were frozen in OCT medium and sectioned using a Cryostat at a thickness of 30 microns for coronal sections or 60 microns for sagittal sections. Immunohistochemistry was performed on free-floating sections. Commercially available primary antibodies to rabbit anti-mouse p-eIF2alpha (1:100, Abcam, cat# ab32157; RRID: AB_732117), goat anti-mouse Choline acetyltransferase (ChAT) (1:200, Millipore, cat# AB144P; RRID: AB_2079751), chicken anti-mouse Tyrosine Hydroxylase (TH) (1:500, Abcam cat# ab76442; RRID: AB_1524535), goat anti-mouse DARPP32 (R&D Systems, cat# AF6259; RRID: AB_10641854), anti-Myc tag (1:200, Abcam, cat# ab9106; RRID: AB_307014), rabbit anti-mouse p-PERK (Thr980) (1:1000, Bioss, cat#Bs-3330R; RRID: AB_10855345), and rabbit anti-mouse RFP (1:1000, Rockland antibodies and assays, cat# 600–401-379; RRID: AB_2209751) or chicken anti-mouse RFP (1:500, Novus Biologicals, cat# NBP1–97371; RRID: AB_11139267) were used for these experiments. Corresponding secondary antibodies raised in donkey conjugated to either Alexa Fluor 488, Alexa Fluor 647, or Rhodamine Red were obtained from ThermoFisher Scientific (Invitrogen). Sections were washed three times with 1× PBS plus 0.3% Triton X-100 (PBS-T), blocked for 1 hour at RT in 10% normal donkey serum (NDS) + 1% bovine serum albumin (BSA), followed by incubation for 48 hours at 4°C with constant rotation on an orbital shaker in primary antibody diluted in 5% NDS in PBS-T. The sections were then washed three times with PBS-T and incubated for 1 hour at RT with corresponding secondary antibody in 5% NDS in PBS-T followed by two washes in PBS-T. Tissue sections were then mounted on slides, covered with Invitrogen SlowFade Diamond Antifade Mountant with DAPI (ThermoFisher Scientific), and cover-slips applied.

Image acquisition and processing

To obtain sagittal section images of SPOTlight (Fig. 1C,D), free floating sections were immunostained with primary antibody to red fluorescent protein which cross reacts with tdTomato followed by Rhodamine Red conjugated secondary antibody and then imaged using a Leica DMi8 Andor Dragonfly 505 unit with Borealis illumination spinning disk confocal microscope at 200× magnification. Post-image acquisition stitching was performed on a MSI – Aegis R desktop using Imaris Stitcher with positioning ascertained by the image metadata and post-stitched image processing was performed in FIJI/ImageJ 64

Imaging of samples involving IHC staining was performed using either the Zeiss Axio Observer for single plane images at 600X magnification or using a Leica Dmi8 Andor Dragonfly 505 unit with Borealis illumination spinning disk confocal microscope at 400X magnification for Z-stacks. Neuronal somatic fluorescent intensity was measured using FIJI analysis software (imagej.nih.gov) by generating a mask to the threshold intensity of the cellular marker (or EGFP for CA2 pyramidal cell and cerebellar Purkinje cell analysis) and selecting each individual soma as a region of interest (ROI) using the wand selection tool with the nuclei excluded. Corrected total cell fluorescence (CTCF) was calculated based on

the measured Integrated Density minus (Area of the selected cell x Mean fluorescence of background readings). For ratiometric analysis, acquisition of EGFP and RFP signal was performed at equal exposure lengths across fluorophores and post-processed in ImageJ using similar settings including background subtraction with rolling ball radius of 50.0 pixels and threshold set to EGFP signal. Masks to EGFP and tdTomato signal were generated and the wand selection tool was used to select regions of interest (individual soma with nuclei excluded). Data are shown as ratios of individual cell CTCF tdTomato/αRFP to CTCF of EGFP signal.

Gi DREADDs

Chemogenetic manipulation of CIN activity was achieved through stereotactic injection of 600 nL of rAAV9-hSyn-DIO-hM4Di mCherry Gi DREADD [plasmid: #44362] (56) or rAAV9-hSyn-DIO-mCherry control (DREADD naïve) [plasmid #50459] obtained from Addgene (Watertown, MA) into the dorsal striatum (anteroposterior +0.7 mm and 2.4 mm mediolateral to bregma at a depth of −3.0 mm) of 10–12-week old ChAT-Cre heterozygous mice. Three weeks after viral delivery, the DREADD agonist, clozapine N-oxide (CNO) was injected i.p. 3 mg/kg/day in two divided doses spaced 8 hours apart for 5 days. On the 5^{th} day, mice were sacrificed 60 minutes following the last dose of CNO by transcardial perfusion for subsequent immunohistochemistry.

Slice electrophysiology

Adult mice (3–8 weeks) were anesthetized and intracardially perfused with high-sucrose solution (194 mM sucrose, 30 mM NaCl, 4.5 mM KCl, 2 mM $MgCl_2$, 0.2 mM $CaCl_2$, 1.2 mM NaH_2PO_4, 26 mM $NaHCO_3$, and 10 mM glucose, saturated with 95% O2 and 5% CO_2). Animals were then decapitated, their brains dissected, and 300 μm coronal slices were cut on a Leica VT1200S vibratome. Slices were transferred to artificial cerebrospinal fluid (ACSF; 124 mM NaCl, 2.5 mM KCl, 1 mM $MgCl_2$, 2 mM $CaCl_2$, 26 mM $NaHCO_3$, 1.2 mM NaH_2PO_4, and 10 mM glucose, saturated with 95% O_2 and 5% CO_2, pH 7.4, 300 mOsm/l) containing test compound or vehicle control and allowed to equilibrate for at least 1 h. Single slices were transferred to a recording chamber and superfused continuously with ACSF containing 50 μM picrotoxin at 32°C and 3–4 mL/min. Neurons were visualized using infrared differential interference microscopy. Micropipettes were pulled (Narishige pc 100) from borosilicate glass tubes (King Precision Glass) for a final resistance of 3 – 4.5 MΩ when filled with internal solution (130 mM KSO_4CH_4, 5 mM KCl, 5 mM NaCl, 100 μM EGTA, 10 mM HEPES, 2 mM $MgCl_2$, 50 μM $CaCl_2$, 2 mM ATP-Mg, 400 μM GTP-Na, pH 7.3, 290 mOsm/l). Cholinergic interneurons in the dorsolateral striatum were first recorded in cell-attached mode. After 15 min baseline recording in test compound/control, slices were treated with 10 μM quinpirole (a selective D2R agonist) (Tocris Bioscience, Minneapolis, MN) for 3 min and recorded for another 12 min thereafter. Afterwards, recording was switched to whole-cell configuration, and the standard I-V protocol was applied for electrophysiological properties to secondarily indicate cell-type. Firing rates were calculated from the 10 minute periods just prior to (“pre”) and immediately following (“post”) quinpirole addition.

Drugs used for slice electrophysiology treatment were stored as stock solutions and working solutions were prepared prior to each experiment and added to the perfusion solution in the final concentration indicated. Apamin (100 nM; Cat. No. 1652); trans-ISRIB (50nM; Cat. No. 5284); AMG PERK 44 (100nM; Cat. No. 5517); CyPPA (20μM; Cat. No. 2953); (RS)-(±)-Sulpiride (5 μM; CAS 156–16-1) and (−)-Quinpirole hydrochloride (10 μM; Cat. No. 1061) from Tocris Bioscience (Bristol, UK). Picrotoxin (50 μM; CAS 124–87-8) from MilliporeSigma (St. Louis, MO).

AAV5-dLight 1.2 injections

Stereotaxic injections were carried out on 1–2 month-old ChAT-Cre mice under isoflurane anesthesia. Meloxicam (5 mg/kg) was administered subcutaneously after anesthesia induction for postoperative pain relief. Craniotomies were made over the injection sites and 600 nL virus were delivered bilaterally to dorsolateral striatum via a Nanoject III (Drummond Scientific) at a rate of 0.2 mL/min. Animals were injected with either 1:1 AAV5 - dLight 1.2 (pAAV-hSyn-dLight1.2, Addgene 111068, $4.8*10^8$ vg/hemisphere) and CReP OE virus (AAV5-hSYN-DIO-mCReP, $3*10^9$ vg/hemisphere) or 1:1 AAV_5 - dLight 1.2 and sterile filtered PBS. The injection pipette was held in place for 10 min following injection and then slowly removed. Coordinates for all injections relative to bregma were as follows: A/P: 0.9 mm, M/L: +/−2.35 mm, D/V: −3.3 and −3.0 mm (300 nL per depth).

dLight1.2 multiphoton imaging

To measure evoked dopamine release, ChAT-Cre animals previously injected with DLight1.2 +/− CReP OE were sacrificed for slice imaging 3–4 weeks post injection. Experimenters were blinded to the viral injection the animals previously received. 300 μm acute coronal slices containing the striatum were prepared as described for electrophysiology with slight modifications; for these experiments, an N-methyl-D-glucamine (NMDG) based ACSF solution was used for perfusion, cutting, and an additional heated recovery step. NMDG ACSF contained (in mM) 90 NMDG, 2.5 KCl, 1.2 NaH_2PO_4, 35 $NaHCO_3$, 20 HEPES, 25 glucose, 5 sodium ascorbate, 2 thiourea, 3 sodium pyruvate, 10 $MgSO_4$ heptahydrate, and 0.5 $CaCl_2$ dihydrate. Immediately after cutting, slices were placed in a 32°C recovery chamber containing NMDG ACSF for 10–12 minutes. After heated recovery, slices were transferred to a chamber containing ACSF for 1 hour at room temperature prior to recording.

Following recovery, slices were placed in a perfusion chamber identical to those used in electrophysiology experiments and similarly superfused with oxygenated ACSF. Slices were visualized using a Bruker Investigator Multiphoton Imaging system under epifluorescence illumination to initially locate a region of interest. A concentric bipolar electrode (FMC) was placed in the dorsal striatum on the lateral side of the estimated dorsomedial/dorsolateral boundary.

After selecting a region of interest, subsequent imaging of dLight1.2 was performed using 920 nm light emitted from a Coherent Comeleon I Ti:Sapphire femtosecond laser to excite dLight1.2 fluorophores. Laser intensity was kept constant across all experiments. Resonant scanned 512 × 512 rasters of the entire FOV were imaged at 30Hz. Fluorescence signal was collected using a Nikon CFI75 LWD 16X W Objective and Quad GaAsP PMTs. Sample

signal was split into red and green channels via a 565lpxr dichroic mirror; dLight1.2 signal was isolated using a 525/70 bandpass PMT filter. ROI selection was refined in real time to maximize visualization of evoked dLight1.2 responses estimated using a single 900 uA electrical test pulse. Electrical stimuli were delivered using an ISO-FLEX Stim Isolation Unit.

Stim-pulse experiments were comprised of repeated 15 × 5 second (150 frames) imaging epochs paired with an electrical pulse (900 uA, 0.3 ms duration) 1 second following the start of image capture. Pulses consisted of, in order, a single stimulation, a 2 Hz, 5 Hz, and 100 Hz stim train (5 pulses each), and a second single pulse. Each stimulation pulse was performed in triplicate for a total of 15 stimulations per condition, and each epoch was separated by a one-minute inter-stim interval. Following acquisition in vehicle (ACSF) conditions, 5 uM sulpiride (Tocris) was added to the chamber and allowed to perfuse for five minutes prior to performing a second imaging sequence. Sulpiride was kept in the bath for the duration of the second session. Tubing and perfusion chamber were cleaned with 70% ethanol and milliQ H_2O between experimental samples.

Following acquisition, imaging files were processed using ImageJ. Regions of interest were drawn over the FOV to include only striatal tissue and exclude the stimulation electrode. ROIs were kept identical across ACSF and sulpiride conditions for each slice. Mean fluorescence intensity for all frames was measured and exported for subsequent analysis in Microsoft Excel, ClampFit (Axon Instruments), and GraphPad Prism. Following extraction, change in raw fluorescence signal (dF) was calculated from baseline fluorescence (F_0), which was taken as the mean intensity of the 1 second pre-stim period of each imaging session, and converted to percentages (dF/F_0*100). dF/F_0 (%) time courses were imported into ClampFit to analyze waveform properties. Peak and area under the curve (AUC) were measured in same time window in all experiments; values for each pulse were taken in triplicate and averaged within each experiment. When comparing dLight1.2 signal amplitude/AUC following stimulation-evoked DA release, each value in sulpiride was normalized to its analogous value in ACSF conditions [i.e. 100 Hz: Peak[sulpiride]/Peak[ACSF]. A total of 4 WT (13 slice experiments) and 3 CReP OE animals (10 slice experiments) were used. For statistical measurement of CReP OE impact on evoked dLight1.2 signal, a two-way ANOVA was used; significance was set at $\alpha = 0.05$. To ensure any observed changes in signal amplitude/AUC was not due to rundown, signal decay was calculated as peak dF/F_0 (%) of the second single stim trial as a percent of the first signal stim trial for each experiment in each condition. There was no apparent signal decay in either condition, and calculated decay metrics were not different across groups (In ACSF: WT [109.8 ± 9.063 SEM, n=14] vs. CReP OE [95.52 ± 2.907 SEM, n=10], p=0.211, unpaired t-test. Sulpiride: WT [99.17 ± 8.668 SEM, n=14] vs. CReP OE [94.22 ± 4.498 SEM, n=10], p = 0.657, unpaired t-test).

Morris Water Maze

For the “weak training protocol”: Mice were trained in a water pool of ~100 cm diameter with a hidden platform of ~10 cm diameter. Mice were handled daily for 3 days before the experiment, and the training protocol consisted of one swimming trial per day. Each mouse

should swim until it finds the hidden platform or 120 s, when it is to be gently guided to the platform and allowed to stay there for 10 s before being returned to the home cage. For the probe test, the platform is removed and each mouse is allowed to swim for 60 s, while its swimming trajectory is monitored with a video tracking system and analysis with Noldus EthoVision XT software (Noldus Information Technology Inc.; RRID: SCR_000441) (20).

Open Field

Mice were placed in an opaque 20 cm x 20 cm open field apparatus and locomotor activity over the course of thirty minutes in five-minute bins. Total distance traveled and velocity were analyzed using Digiscan analyses (Accuscan Instruments).

Operant Chamber Lever Press

Prior to the start of training, animals were food restricted over 3 days to 85–90% of their baseline weight to motivate learning. All animals were maintained at this restricted weight for the duration of their training. All training and testing occurred in Med Associates operant chambers housed within light-resistant, sound-attenuating cabinets (ENV-022MD). During each training and testing session, mice were presented with 2 levers – one lever on the left and one on the right of the food cup. On training days, only lever presses on the left lever were rewarded with sucrose-containing pellets (Bio-serv, F05684). Lever presses and food cup entries were recorded by Med-PC-V software (Med Associates Inc. RRID: SCR_012156). Food cup entries were detected by the breaking of an infrared beam inside the cup.

Animals were trained on the schedule described in Figure 5B. Mice started training with 5 days of continuous reinforcement (CRF) in which each left lever press results in reward. CRF sessions lasted 60 minutes or until the mice received 100 reinforcers. CRF is used to establish the association between the left lever press action and the sucrose pellet outcome. After CRF, animals were trained in random interval (RI) reinforcement schedules, with all training sessions lasting 60 minutes or until mice received 50 reinforcers. After the last session of CRF, mice were given 3 sessions of random interval 30 (RI-30) schedule followed by 8 days of random interval 60 (RI-60) schedule. RI reinforcement resulted in a 10% chance that a sugar pellet would be available each X/10 seconds for a RI-X schedule. For example, in an RI-60 schedule, for each 6 second epoch, there was a 10% chance that a pellet would be delivered the next time the lever was pressed. In simpler terms, this means that on average one reinforcer is delivered upon the first press after 60 seconds since the last reinforcer was given. This random interval schedule weakens the behavior-reward relationship, biasing the action of a lever press towards being established as a habit. Following RI reinforcement training, mice underwent devaluation testing with an extinction probe test to measure habitual behavior as previously described (41). All training was performed with experimenter blinded to viral expression group.

Experimental Blinding and Statistical Analysis

Sample size: Sample size used for any measurement was based on the ARRIVE recommendations on refinement and reduction of animal use in research. Minimal sample sizes were estimated based on previously published work, author's experience, and our

preliminary investigations. In experiments that were repeated with different perturbations as in Fig. 3, power analysis was used to establish minimum group sizes. **Replication:** In all experiments, a minimum of two to three independent biological replicates of mice were used. All attempts at replication were successful. At the animal subject level, at least 3 mice were used in each experimental group, with the exception of one experimental group with 2 mice. Replicates are fully described in manuscript to include independent mice and cells. **Randomization:** For animal studies, mice were randomized to achieve balance of age, sex and littermates across groups. All other experimental variables, such as viral type or chemical compounds were blinded and randomized across groups. Whenever possible, both treatment groups were tested at the same time. When both conditions were not possible to test on the same day, treatment groups were interleaved on alternating days. **Blinding:** The test experimental variable was blinded for all experiments reported to experimental group (eg genotype, genetic manipulation/virus, or drug treatment). Data unblinding was performed once data analysis including quality control and exclusion criteria assessment was completed and documented. **Data exclusions:** Samples or animals were excluded rarely (<10% of collected). Exclusions occurred for technical reasons as in the case of incorrect/absent stereotaxic viral targeting, inadequate fixative perfusion of animals impairing immuno-labeling of histological sections, or when cells in electrophysiological recordings did not meet pre-established exclusion criteria related to cell identity and recording stability. All data exclusions were made prior to unblinding. When numerical data were transformed to Log2 ratio in Figure 3, if no firing was detected in the post-quinpirole period, an imputed value was used equivalent to a single event occurring (0.00166 Hz, e.g. 1 AP in 601 s) in place of zero to avoid NaN; The number of such imputed values are indicated in parentheses - Fig. 3D Veh (3), ISRIB (1); Fig. 3M Cre(−) (2). **Statistical analysis:** Data shown as mean ± SEM. The evaluation of statistical differences was performed with nested t-tests throughout manuscript with a few exceptions noted in figure legends. Data acquired from immunohistochemistry studies were analyzed using GraphPad Prism 9.0 by two-tailed nested t-test or nested one-way ANOVA with Tukey's post-hoc analysis where appropriate for p-value and F-statistic. For slice electrophysiology data analysis, data were acquired by pClamp v10.7 and analyzed using pClampfit v10.7 (Molecular Device; RRID: SCR_011323), Origin 8.0 (Microcal; RRID: SCR_002815), Prism 9.0 (GraphPad: RRID: SCR_002798), and MATLAB R2018a (The MathWorks, Inc.; RRID: SCR_001622). For single-cell sequencing data analysis, differential *Atf4* expression was evaluated by two-tailed t-test with Welch's correction. For behavioral testing, latency to escape and velocity during the Morris Water Maze task, velocity during the Open Field test and lever press rate between experimental groups was compared by Two-way repeated measures ANOVA with Sidak's post hoc test for multiple comparisons, NDLPr by unpaired t-test, and Inter-Press Interval by two-way Kolmogorov-Smirnov (K-S) test for probability distribution. For all analyses, data is shown as mean ± SEM and the significance level set at $p < 0.05$.

Supplementary Material

Refer to Web version on PubMed Central for supplementary material.

ACKNOWLEDGMENTS:

We wish to thank Katja Brose, Helene Marie, Ben Philpot, and Jim McNamara for their input on the manuscript. We wish to acknowledge Alyssa Florwick, Rachel Settelen, Kaylin Tsukayama, Tal Greber, Christopher R. Means, and Ramona M. Rodriguiz for technical assistance. A substantial portion of this study occurred under the hardships of the COVID-19 pandemic. We are grateful to the researchers and staff who made this possible.

Funding:

Research was supported by funding from the following sources: NIH BRAIN initiative (NS110059, N.C.; MH123017, B.D.T.), NIH (NS076708–06, M.C.-M.; NS051156 and NS095653, J.E.R.), NSF (DGE-1644868, V.L.H.), Dystonia Medical Research Foundation (N.C., A.R.H.), Tyler's Hope for a Dystonia Cure (N.C.) and Holland-Trice Scholar award (N.C.).

REFERENCES AND NOTES

1. Pakos-Zebrucka Ket al., The integrated stress response. EMBO Rep. 17, 1374–1395 (2016). [PubMed: 27629041]
2. Harding HPet al., An integrated stress response regulates amino acid metabolism and resistance to oxidative stress. Mol. Cell11, 619–633 (2003). [PubMed: 12667446]
3. Trinh MA, Klann E, Translational control by eIF2α kinases in long-lasting synaptic plasticity and long-term memory. Neurobiol. Learn. Mem105, 93–99 (2013). [PubMed: 23707798]
4. Costa-Mattioli M, Sossin WS, Klann E, Sonenberg N, Translational control of long-lasting synaptic plasticity and memory. Neuron. 61, 10–26 (2009). [PubMed: 19146809]
5. Costa-Mattioli M, Walter P, The integrated stress response: From mechanism to disease. Science. 368, eaat5314 (2020). [PubMed: 32327570]
6. Rittiner JEet al., Functional genomic analyses of mendelian and sporadic disease identify impaired eIF2α signaling as a generalizable mechanism for dystonia. Neuron. 92, 1238–1251 (2016). [PubMed: 27939583]
7. Halliday Met al., Repurposed drugs targeting eIF2alpha-P-mediated translational repression prevent neurodegeneration in mice. Brain. 140, 1768–1783 (2017). [PubMed: 28430857]
8. Segev Yet al., PKR inhibition rescues memory deficit and atf4 overexpression in apoe ε4 human replacement mice. J. Neurosci35, 12986–12993 (2015). [PubMed: 26400930]
9. Wong YLet al., The small molecule ISRIB rescues the stability and activity of vanishing white matter disease eIF2B mutant complexes. Elife. 7, e32733 (2018). [PubMed: 29489452]
10. Cagnetta Ret al., Noncanonical modulation of the eIF2 pathway controls an increase in local translation during neural wiring. Mol. Cell73, 474–489.e5 (2019). [PubMed: 30595434]
11. Moreno JAet al., Sustained translational repression by eIF2α-P mediates prion neurodegeneration. Nature. 485, 507–511 (2012). [PubMed: 22622579]
12. Kabir ZDet al., Rescue of impaired sociability and anxiety-like behavior in adult cacna1c-deficient mice by pharmacologically targeting eIF2α. Mol. Psychiatry22, 1096–1109 (2017). [PubMed: 28584287]
13. Mao Det al., De novo EIF2AK1 and EIF2AK2 variants are associated with developmental delay, leukoencephalopathy, and neurologic Decompensation. Am. J. Hum. Genet106, 570–583 (2020). [PubMed: 32197074]
14. Huang Wet al., Translational control by eIF2α phosphorylation regulates vulnerability to the synaptic and behavioral effects of cocaine. Elife. 5, e12052 (2016). [PubMed: 26928234]
15. Colla Eet al., Endoplasmic reticulum stress is important for the manifestations of-synucleinopathy in vivo. J. Neurosci32, 3306–3320 (2012). [PubMed: 22399753]
16. Wek RC, Role of eIF2α kinases in translational control and adaptation to cellular stress. Cold Spring Harb. Perspect. Biol10, a032870 (2018). [PubMed: 29440070]
17. Harding HPet al., Regulated translation initiation controls stress-induced gene expression in mammalian cells. Mol. Cell6, 1099–1108 (2000). [PubMed: 11106749]
18. Vattem KM, Wek RC, Reinitiation involving upstream ORFs regulates ATF4 mRNA translation in mammalian cells. Proc. Natl. Acad. Sci. U. S. A101, 11269–11274 (2004). [PubMed: 15277680]

19. S. R. Starck et al., Translation from the 5’ untranslated region shapes the integrated stress response. Science. 351, aad3867 (2016). [PubMed: 26823435]
20. Sidrauski Cet al., Pharmacological brake-release of mRNA translation enhances cognitive memory. Elife. 2013, e00498 (2013).
21. Costa-Mattioli Met al., eIF2α Phosphorylation bidirectionally regulates the switch from short- to long-term synaptic plasticity and memory. Cell. 129, 195–206 (2007). [PubMed: 17418795]
22. Zhu PJet al., Suppression of PKR promotes network excitability and enhanced cognition by interferon-γ-mediated disinhibition. Cell. 147, 1384–1396 (2011). [PubMed: 22153080]
23. Vattem KM, Wek RC, Reinitiation involving upstream ORFs regulates ATF4 mRNA translation in mammalian cells. Proc. Natl. Acad. Sci. U. S. A101, 11269–11274 (2004). [PubMed: 15277680]
24. Chan KYet al., Engineered AAVs for efficient noninvasive gene delivery to the central and peripheral nervous systems. Nat. Neurosci20, 1172–1179 (2017). [PubMed: 28671695]
25. Zyryanova AFet al., ISRIB blunts the integrated stress response by allosterically antagonising the inhibitory effect of phosphorylated eIF2 on eIF2B. Mol. Cell81, 88–103.e6 (2021). [PubMed: 33220178]
26. Cheng J, Umschweif G, Leung J, Sagi Y, Greengard P, HCN2 channels in cholinergic interneurons of nucleus accumbens shell regulate depressive behaviors. Neuron. 101, 662–672.e5 (2019). [PubMed: 30638901]
27. Armbruster BN, Li X, Pausch MH, Herlitze S, Roth BL, Evolving the lock to fit the key to create a family of G protein-coupled receptors potently activated by an inert ligand. Proc. Natl. Acad. Sci. U.S.A104, 5163–5168 (2007). [PubMed: 17360345]
28. Di Prisco GVet al., Translational control of mGluR-dependent long-term depression and object-place learning by eIF2α. Nat. Neurosci17, 1073–1082 (2014). [PubMed: 24974795]
29. Augustin SM, Chancey JH, Lovinger DM, Dual dopaminergic regulation of corticostriatal plasticity by cholinergic interneurons and indirect pathway medium spiny neurons. Cell Rep. 24, 2883–2893 (2018). [PubMed: 30208314]
30. Wang Zet al., Dopaminergic control of corticostriatal long-term synaptic depression in medium spiny neurons is mediated by cholinergic interneurons. Neuron. 50, 443–452 (2006). [PubMed: 16675398]
31. Maurice Net al., D2 dopamine receptor-mediated modulation of voltage-dependent Na+ channels reduces autonomous activity in striatal cholinergic interneurons. J. Neurosci24, 10289–10301 (2004). [PubMed: 15548642]
32. Aosaki T, Miura M, Suzuki T, Nishimura K, Masuda M, Acetylcholine-dopamine balance hypothesis in the striatum: An update. Geriatr. Gerontol. Int10, S148–S157 (2010). [PubMed: 20590830]
33. Lovinger DM, Neurotransmitter roles in synaptic modulation, plasticity and learning in the dorsal striatum. Neuropharmacology. 58, 951–961 (2010). [PubMed: 20096294]
34. Scheuner Det al., Translational control is required for the unfolded protein response and in vivo glucose homeostasis. Mol. Cell7, 1165–1176 (2001). [PubMed: 11430820]
35. Goldberg JA, Teagarden MA, Foehring RC, Wilson CJ, Nonequilibrium calcium dynamics regulate the autonomous firing pattern of rat striatal cholinergic interneurons. J. Neurosci29, 8396–8407 (2009). [PubMed: 19571130]
36. Goldberg JA, Wilson CJ, B, Control of spontaneous firing patterns by the selective coupling of calcium currents to calcium-activated potassium currents in striatal cholinergic interneurons. J. Neurosci25, 10230–10238 (2005). [PubMed: 16267230]
37. Threlfell Set al., Striatal dopamine release is triggered by synchronized activity in cholinergic interneurons. Neuron. 75, 58–64 (2012). [PubMed: 22794260]
38. Patriarchi Tet al., Ultrafast neuronal imaging of dopamine dynamics with designed genetically encoded sensors. Science. 360, eaat4422 (2018). [PubMed: 29853555]
39. Shin JH, Adrover MF, Alvarez VA, Distinctive modulation of dopamine release in the nucleus accumbens shell mediated by dopamine and acetylcholine receptors. J. Neurosci37, 11166–11180 (2017). [PubMed: 29030431]
40. Pisani A, Bernardi G, Ding J, Surmeier DJ, Re-emergence of striatal cholinergic interneurons in movement disorders. Trends Neurosci. 30, 545–553 (2007). [PubMed: 17904652]

41. O'Hare JKet al., Pathway-specific striatal substrates for habitual behavior. Neuron. 89, 472–479 (2016). [PubMed: 26804995]
42. O'Hare JKet al., Striatal fast-spiking interneurons selectively modulate circuit output and are required for habitual behavior. Elife. 6, e26231 (2017). [PubMed: 28871960]
43. Hilário MRF, Clouse E, Yin HH, Costa RM, Endocannabinoid signaling is critical for habit formation. Front. Integr. Neurosci1 (2007), doi:10.3389/neuro.07.006.2007.
44. Panigrahi Bet al., Dopamine is required for the neural representation and control of movement vigor. Cell. 162, 1418–1430 (2015). [PubMed: 26359992]
45. Beierholm Uet al., Dopamine modulates reward-related vigor. Neuropsychopharmacology. 38, 1495–1503 (2013). [PubMed: 23419875]
46. Pathak SSet al., The eIF2α kinase GCN2 modulates period and rhythmicity of the circadian clock by translational control of Atf4. Neuron. 104, 724–735.e6 (2019). [PubMed: 31522764]
47. Witten IBet al., Cholinergic interneurons control local circuit activity and cocaine conditioning. Science. 330, 1677–1681 (2010). [PubMed: 21164015]
48. Warner-Schmidt JLet al., Cholinergic interneurons in the nucleus accumbens regulate depression-like behavior. Proc. Natl. Acad. Sci. U. S. A109, 11360–11365 (2012). [PubMed: 22733786]
49. Nguyen HGet al., Development of a stress response therapy targeting aggressive prostate cancer. Sci. Transl. Med10, eaar2036 (2018). [PubMed: 29720449]
50. Sutton MA, Schuman EM, Dendritic protein synthesis, synaptic plasticity, and memory. Cell. 127, 49–58 (2006). [PubMed: 17018276]
51. Picciotto MR, Higley MJ, Mineur YS, Acetylcholine as a neuromodulator: Cholinergic signaling shapes nervous system function and behavior. Neuron. 76, 116–129 (2012). [PubMed: 23040810]
52. Conner JM, Culberson A, Packowski C, Chiba AA, Tuszynski MH, Lesions of the basal forebrain cholinergic system impair task acquisition and abolish cortical plasticity associated with motor skill learning. Neuron. 38, 819–829 (2003). [PubMed: 12797965]
53. Tritsch NX, Sabatini BL, Dopaminergic modulation of synaptic transmission in cortex and striatum. Neuron. 76, 33–50 (2012). [PubMed: 23040805]
54. Mansvelder HD, Mcgehee DS, Long-term potentiation of excitatory inputs to brain reward areas by nicotine. Neuron. 27, 349–357 (2000). [PubMed: 10985354]
55. Rossi Jet al., Melanocortin-4 receptors expressed by cholinergic neurons regulate energy balance and glucose homeostasis. Cell Metab. 13, 195–204 (2011). [PubMed: 21284986]
56. Krashes MJet al., Rapid, reversible activation of AgRP neurons drives feeding behavior in mice. J. Clin. Invest121, 1424–1428 (2011). [PubMed: 21364278]
57. Belleau ML, Warren RA, Postnatal development of electrophysiological properties of nucleus accumbens neurons. J. Neurophysiol84, 2204–2216 (2000). [PubMed: 11067966]
58. Bennett BD, Callaway JC, Wilson CJ, Intrinsic membrane properties underlying spontaneous tonic firing in neostriatal cholinergic interneurons. J. Neurosci20, 8493–8503 (2000). [PubMed: 11069957]
59. Kawaguchi Y, Large aspiny cells in the matrix of the rat neostriatum in vitro: Physiological identification, relation to the compartments and excitatory postsynaptic currents. J. Neurophysiol67, 1669–1682 (1992). [PubMed: 1352806]
60. Kawaguchi Y, Physiological, morphological, and histochemical characterization of three classes of interneurons in rat neostriatum. J. Neurosci13, 4908–4923 (1993). [PubMed: 7693897]
61. Park YGet al., Protection of tissue physicochemical properties using polyfunctional crosslinkers. Nat. Biotechnol37, 73 (2019).
62. Kim SYet al., Stochastic electrotransport selectively enhances the transport of highly electromobile molecules. Proc. Natl. Acad. Sci. U. S. A112, E6274–E6283 (2015). [PubMed: 26578787]
63. Murray Eet al., Simple, scalable proteomic imaging for high-dimensional profiling of intact systems. Cell. 163, 1500–1514 (2015). [PubMed: 26638076]
64. Muñoz-Manchado ABet al., Diversity of interneurons in the dorsal striatum revealed by single-cell RNA sequencing and PatchSeq. Cell Rep24, 2179–2190.e7 (2018). [PubMed: 30134177]
65. Kheirbek MAet al., Adenylyl cyclase type 5 contributes to corticostriatal plasticity and striatum-dependent learning. J. Neurosci29, 12115–12124 (2009). [PubMed: 19793969]

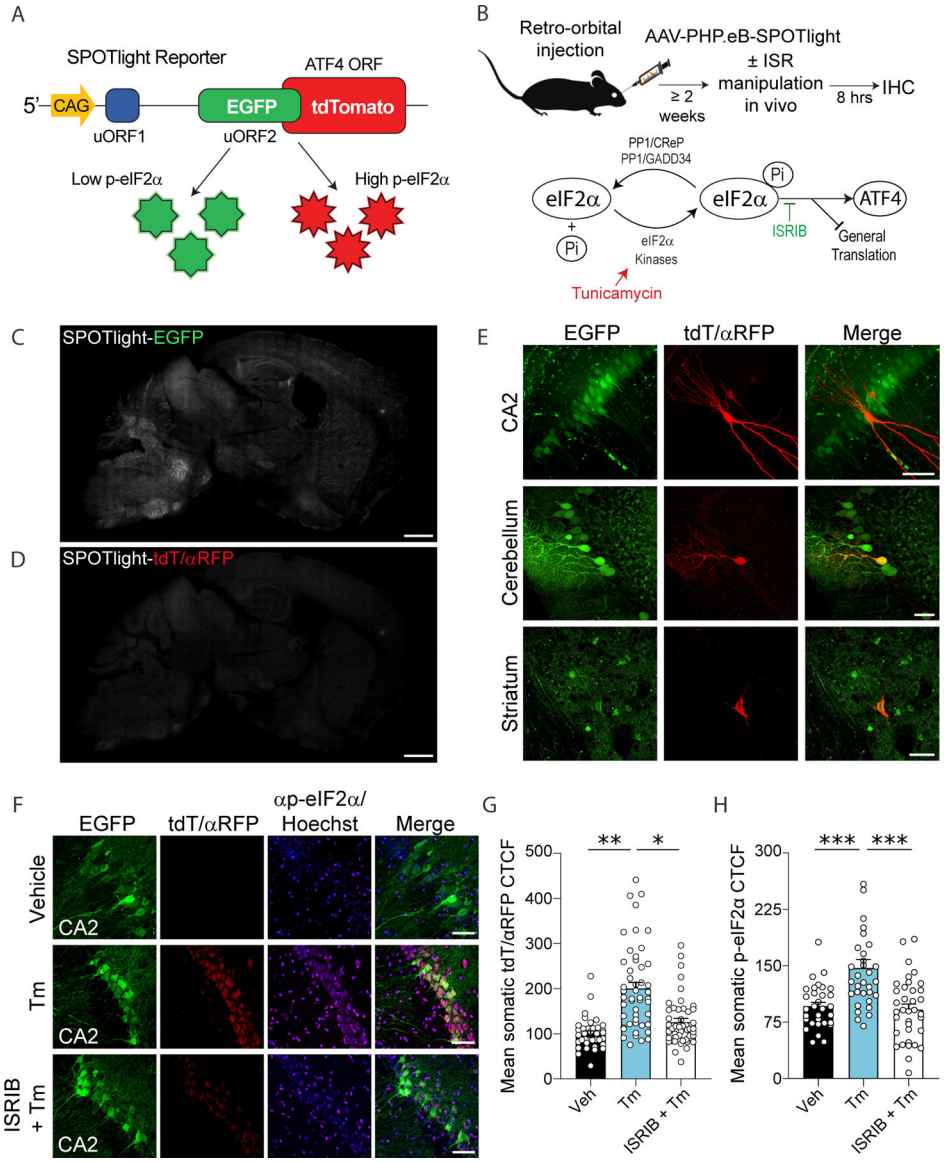

Figure 1. SPOTlight, a brain-wide reporter of ISR state-dependent translation.

(**A**) SPOTlight reporter design. (**B**) *Top* – Brain-wide delivery of SPOTlight reporter and validation strategy. *Bottom* – ISR schematic showing Tunicamycin and ISRIB sites of action. (**C** and **D**) Mid-section sagittal views of brain-wide SPOTlight EGFP (**C**) and tdTomato (**D**) (amplified by anti-RFP with Rhodamine Red-conjugated secondary antibody) expression under basal conditions. Scale bar 1000 microns. (**E**) A survey of the brain reveals rare cells in the hippocampus (scale bar 100 microns), cerebellum and striatum (scale bars 50 microns) with strong tdTomato signal. (**F**) *In vivo* induction of the ISR with acute tunicamycin (middle row) results in a robust increase in tdTomato signal compared to vehicle (top row), which corresponds with p-eIF2α immuno-positive soma in the CA2 pyramidal layer of the mouse hippocampus. This increase is attenuated by pre-treatment with ISRIB (bottom row). Scale bar 50 microns. (**G**) Quantification of tdTomato signal. (Veh - 8 mice, 76 cells; Tm - 9 mice, 137 cells; ISRIB/Tm - 4 mice, 110 cells). Nested t-test for

Tm v Veh: *t=3*.861, F(1,15)=14.91, **p=0.0015; Tm v ISRIB/Tm: *t=2*.612, F(1,11)=6.823, *p=0.0242); and ISRIB/Tm v Veh: *t=1*.000, F(1,10)=1.001, p=0.3407 (ns). Treatment: F(3,20)= 4.788, *p=0.0113 by nested one-way ANOVA with Tukey's post hoc test for multiple comparisons. (**H**) Quantification of mean somatic p-eIF2α corrected total cell fluorescence (CTCF). (Veh - 3 mice, 64 cells; Tm - 3 mice, 77 cells; ISRIB/Tm - 3 mice, 79 cells). Nested t-test for Tm v. Veh: *t=5*.187, F(1,139)= 26.90, ***p=0.0001; ISRIB/Tm v Tm: *t=4*.620, F(1,154)=21.34, ***p<0.0001; and ISRIB/Tm v Veh: *t*=0.409, F(1,141)=0.1675, p=0.6830 (ns). Treatment: F(3,257)=12.19, ***p<0.0001 by nested one-way ANOVA with Tukey's post hoc test for multiple comparisons.

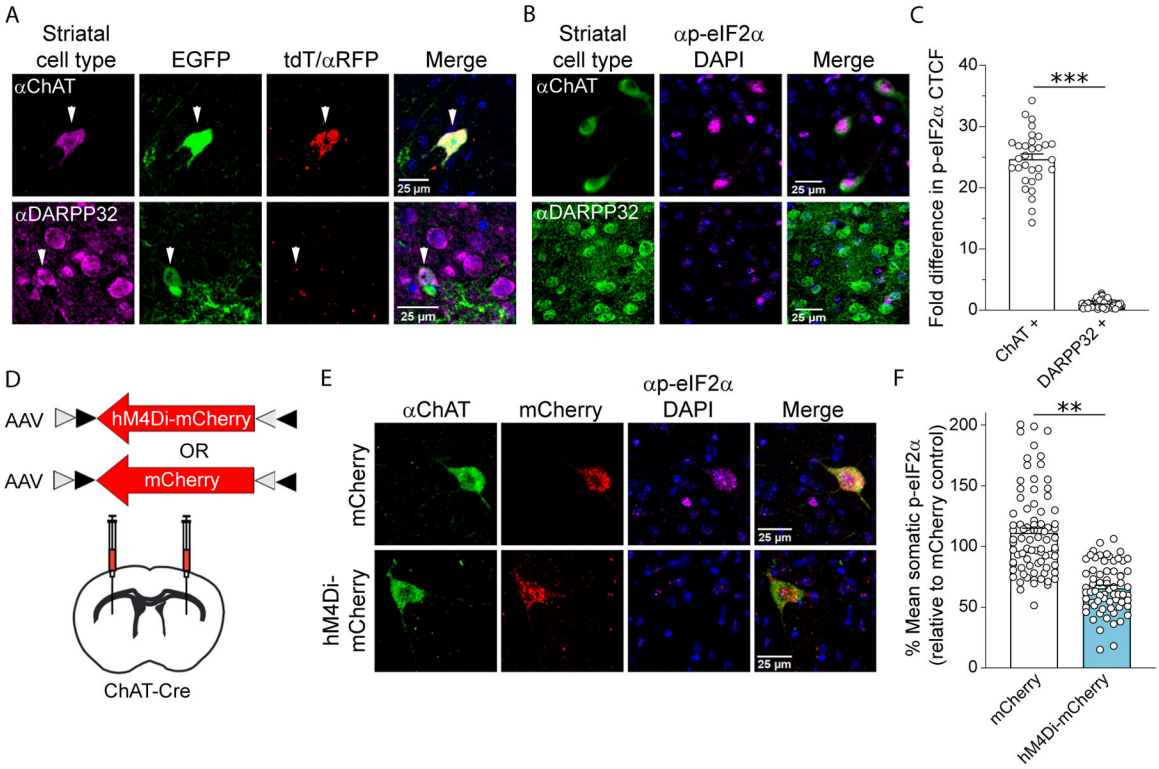

Figure 2. CINs show steady-state activity-dependent ISR activation.

(**A**) Photomicrographs of the dorsal striatum showing levels of SPOTlight EGFP and tdTomato (amplified by anti-RFP/Rhodamine Red) in CINs (ChAT+, top) and SPNs (DARPP32+, bottom). (**B**) Phospho-eIF2α immunofluorescence in CINs (top) and SPNs (bottom). (**C**) Quantification of p-eIF2α CTCF from (**B**). Images were analyzed with FIJI, and immunofluorescence was determined per cell and presented as the mean CTCF ± SEM. (ChAT+ - 3 mice, 92 cells; DARPP32+ - 3 mice, 395 cells). Nested t-test, t=12.54, F(1,4)=157.3, ***p=0.0002. Scale bar 25 microns. (**D**) Strategy for Cre-mediated expression of hM4Di (Gi) DREADD fused to mCherry or mCherry alone in dorsal striatal CINs of ChAT-Cre heterozygous mice. All mice received chronic clozapine-N-oxide (CNO) at a dose of 3 mg/kg/day divided in two evenly spaced doses for 5 days. (**E**) Representative photomicrographs from the dorsal striatum of mCherry control (top) vs Gi DREADD-expressing (bottom) mice showing ChAT immunohistochemistry, mCherry expression, p-eIF2α immunohistochemistry with DAPI counterstain, and merged images. Scale bar 25 microns. (**F**) Quantification of p-eIF2α CTCF from (**E**). (mCherry control - 5 mice, 270 ChAT+ cells; Gi DREADD - 5 mice, 215 ChAT+ cells). Nested t-test: t=4.079, F(1,8)=16.64, **p=0.0035.

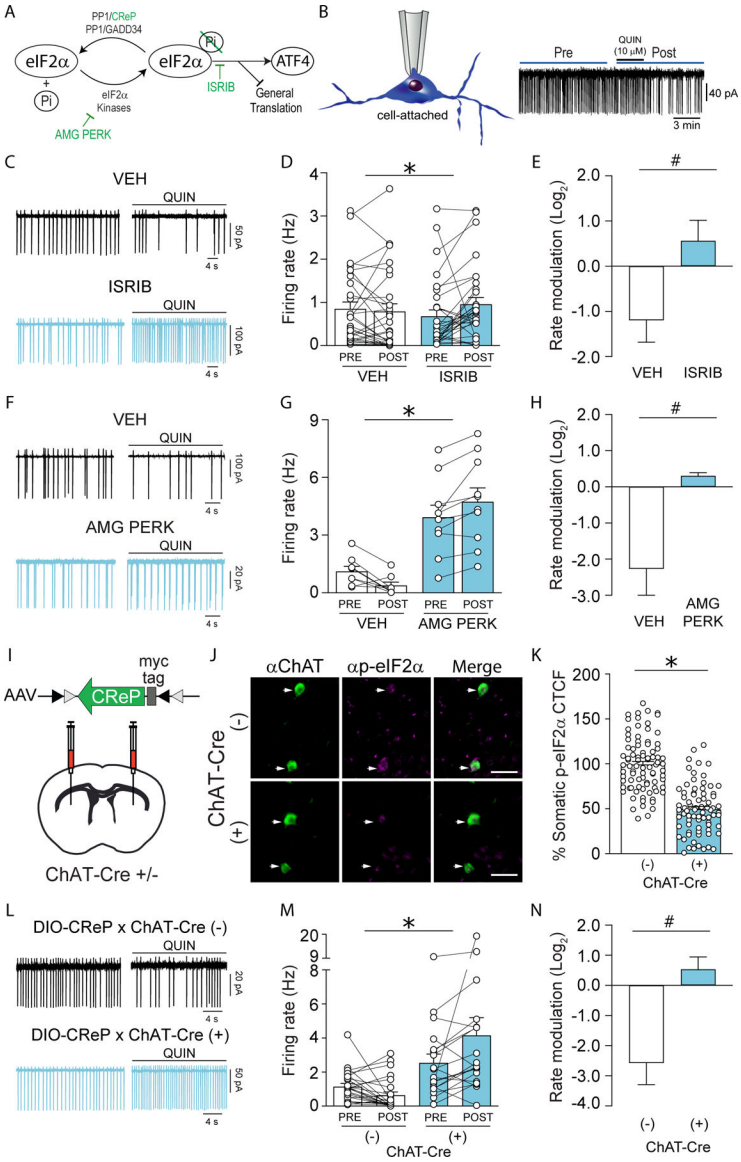

Figure 3. ISR state in CINs alters D2R modulation of CIN firing.

(**A**) ISR schematic showing pharmacological and genetic manipulations in green. (**B**) Illustration of cell-attached recording mode and representative trace displaying the normally observed pause in CIN firing in response to the D2R agonist quinpirole. (**C**) Representative recordings of spontaneous CIN firing before and after quinpirole addition (10 μM, 3 min) in brain slices pre-incubated with vehicle or 50 nM ISRIB. (**D**) Quantification of CIN firing rates, showing paired measurements before and after quinpirole (Veh - 13 mice, 29 cells; ISRIB - 11 mice, 30 cells). Nested t-test: t=2.612, F(1,22)=6.882; *p=0.016. (**E**) Log2 modulation index of data in (**D**), to illustrate net directionality of D2R modulation; rate decreases below the abscissa and increases above it. (**F**) Representative recordings of spontaneous CIN firing before and after quinpirole (10 μM, 3 min) in brain slices pre-incubated with vehicle or 100 nM AMG PERK 44. (**G**) Quantification showing paired measurements before and after quinpirole (Veh - 3 mice, 8 cells; AMG PERK 44 – 3 mice,

10 cells). Nested t-test: t=3.563, F(1,16)=12.70; *p=0.034. (**H**) Log2 modulation index of data in panel (**G**). (**I**) Strategy for Cre-dependent expression of the p-eIF2α phosphatase CReP in CINs (AAV9-DIO CReP x ChAT-Cre mice). (**J**) Example images of ChAT and p-eIF2α immunohistochemistry in CINs (ChAT+ cells). Scale bar 25 microns. (**K**) Quantification of mean somatic p-eIF2α CTCF from (**J**). (Cre(−) - 3 mice, 109 cells; Cre(+) - 3 mice, 94 cells). Nested t-test: t=3.664, F(1,4)=13.42, *p=0.022. (**L**) Representative recordings of spontaneous CIN firing before and after quinpirole (10 μM, 3 min) in CINs over-expressing CReP. (**M**) Quantification of paired measurements before and after quinpirole (Cre(−) - 10 mice, 24 cells; Cre(+) - 9 mice, 19 cells). Nested t-test: t=2.392 F(1,41)=5.720; *p=0.021. (**N**) Log2 modulation index of data in (**M**). $^{\#}$P-values of all Log_2 graphs are < 0.05. Since some of these data include imputed values to avoid NaN (See Materials and Methods), the reader is referred to p-value for the primary data in prior panel.

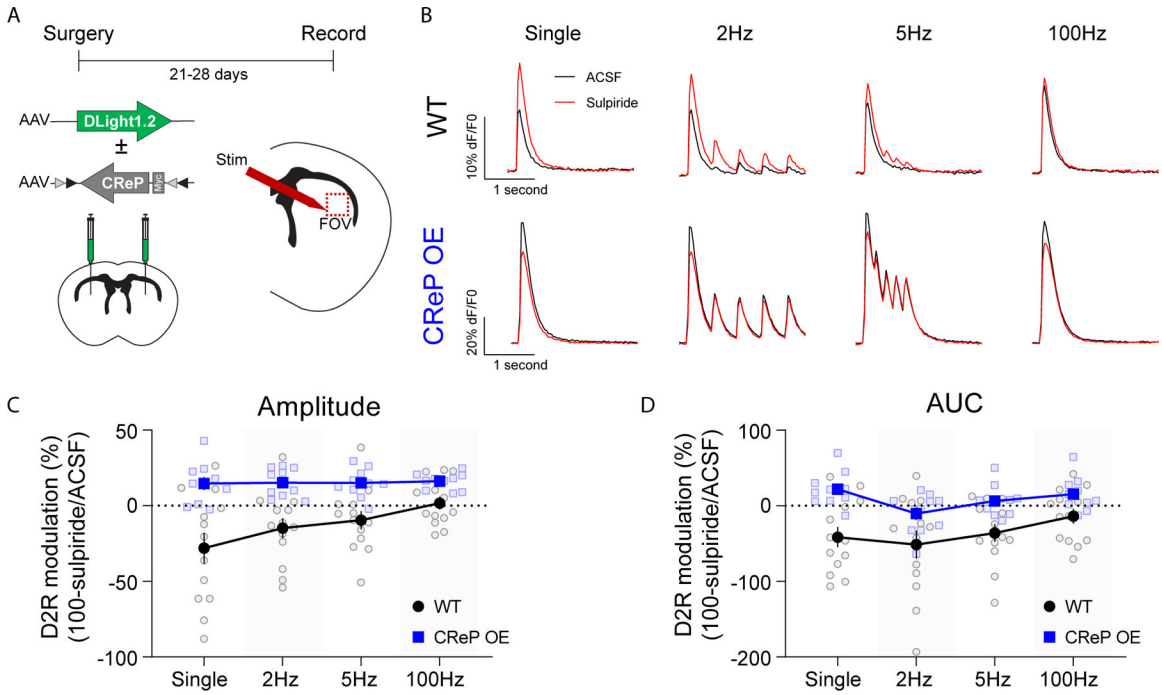

Figure 4. CIN ISR inhibition inverts the effect of D2R modulation on evoked dopamine transients.

(**A**) Schematic illustrating viral expression of dLight1.2 reporter ± Cre-dependent overexpression of CReP in dorsal striatum of ChAT-Cre mice, followed by recording of evoked transients in acute brain slices. FOV indicates recording field of view. (**B**) Representative traces of whole-FOV striatal responses to electrically evoked dopamine release using a single pulse or five pulses at 2, 5, or 100Hz. Example traces are the mean of three responses, and are represented as % dF/F_0 (percent change in baseline fluorescence). Control (top) and CReP-OE (bottom) conditions in ACSF (black) and 5 μM Sulpiride (red). (**C**) Mean effect of D2R modulation on the peak amplitude of evoked dLight1.2 responses, represented as 100 - Amplitude[Sulpiride]/Amplitude[ACSF] (%). Values are mean ± SEM. (Control - 4 mice, 13 slices; CReP-OE - 3 mice, 10 slices). Two-way ANOVA – significant effects of viral manipulation [$F(1,21) = 16.15$, $p<0.001$] and pulse number [$F(1.302, 27.34) = 5.117$, $p<0.05$], and a significant interaction [$F(3,63) = 4.237$, $p<0.01$]. (**D**) Mean effect of D2R modulation on the area under the curve (AUC) of evoked dLight1.2 responses. Values are mean ± SEM. (Control - 4 mice, 13 slices; CReP-OE - 3 mice, 10 slices). Two-way ANOVA – significant effects of viral manipulation [$F(1,21) = 10.87$, $p<0.01$] and pulse number [$F(2.173, 45.64) = 4.730$, $p<0.05$], but no interaction [$F(3,63) = 1.37$, $p=0.26$].

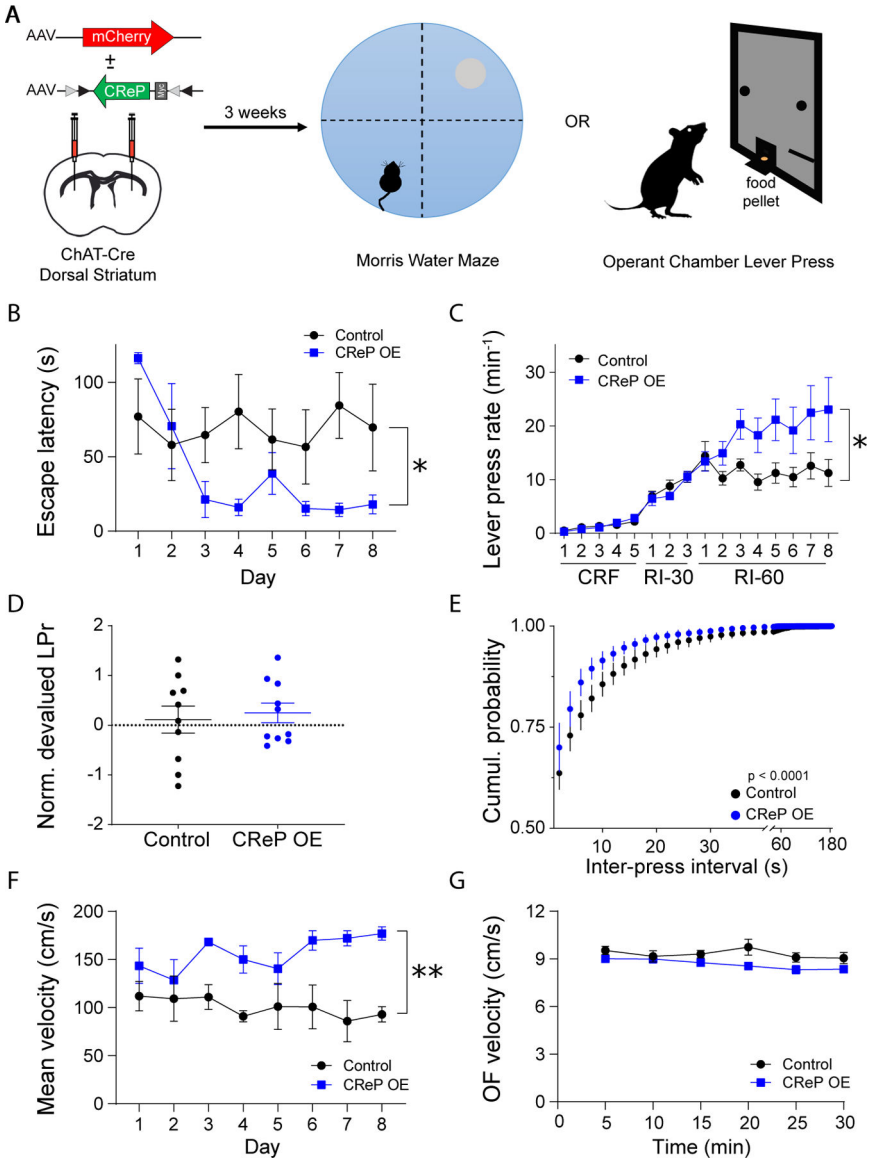

Figure 5. CIN ISR inhibition enhances performance vigor of learned tasks.

(**A**) Schematic illustrating viral expression of mCherry tracer ± Cre-dependent CReP overexpression in dorsal striatum of ChAT-Cre mice (left), followed three weeks later by testing in the Morris water maze (center), operant chamber lever press task (right), and open field (not shown). (**B**) Results of Morris water maze training. Male ChAT-Cre heterozygous mice with CReP OE in dorsal striatal CINs (blue) reached the hidden platform faster than controls (black; mCherry virus alone) over the course of training in a modified Morris water maze protocol as used in [2,29]. (4 mice per group). *p=0.0106 by two-way rmANOVA with Bonferonni's post-hoc test F(7,42)=3.068. (**C**) Results of lever press training. Cre-dependent CReP OE mice (blue) achieved higher lever press rates than control mice (black; mCherry virus alone) in a randomized interval (RI) training protocol using increasing mean time delays before reward delivery. (10 mice per group). Two-way ANOVA with Sidak's multiple comparisons test: F(15,270)=3.776, *p< 0.0001. CRF – continuous reinforcement; RI-30

– random interval, 30s average delay; RI-60 – random interval, 60s average delay. (**D)** Normalized devalued lever press rate (NDLPr), a measure of habit learning, was not affected by CIN CReP overexpression. (10 mice per group; p=0.69). (**E**) Cumulative probability distribution showing CReP OE mice (blue) pressed with shorter intervals between presses than controls (black) on the final day of lever press training. (Control - 7 mice, 5,797 events; CReP OE - 7 mice, 10,841 events; data for 3 mice in each cohort was lost due to instrument failure). *p<0.0001 by two sample Kolmogorov-Smirnov test. (**F)** Mean swimming velocity of mice with CReP OE (blue) exceeded that of mCherry controls (black) during the Morris water maze task. (4 mice per group). Two-way rmANOVA: $F(6,42)=4.981$, $^{**}p=0.0006$. (**G**) CReP OE mice show no differences in locomotor speed during exploration of a novel open field chamber. (10 mice per group). Two-way ANOVA: $F(5,90)=1.645$, $p=0.1563$. All data are presented as mean ± SEM.